Supplementary Information (SI) for Journal of Materials Chemistry A.

Supporting Information

Coupled Influence of State-of-Charge and Storage Temperature on Calendar Aging and Subsequent Cycle Degradation in $LiFePO_4$/Graphite Pouch Cells

Wenjun Shen,[ab] Jinyang Dong,*[ab] Yun Lu,[ab] Kang Yan,[b] Yibiao Guan,*[c] Guangjin Zhao,[d] Bowen Li,[d] Xi Wang,[ab] Rui Tang,[ab] Jialong Zhou,[ab] Ning Li,[ab] Yuefeng Su,*[ab] Feng Wu,[ab] and Lai Chen*[ab]

[a]School of Materials Science and Engineering, Beijing Key Laboratory of Environmental Science and Engineering, Beijing Institute of Technology, Beijing 100081, China.

[b]Chongqing Innovation Center, Beijing Institute of Technology, Chongqing 401120, China.

[c]China Electric Power Research Institute, Beijing 100192, China.

[d]State Grid Henan Electric Power Research Institute, Zhengzhou 450052, China.

Experimental Sections

Electrochemical measurements

$LiFePO_4$/graphite pouch-type lithium-ion batteries were provided by Contemporary Amperex Technology Co., Limited (CATL), with a nominal capacity of 110 mAh. Each cell consisted of one double-sided graphite anode and two single-sided $LiFePO_4$ cathodes, with electrode dimensions of 43.5 × 51.0 mm (anode) and 42.0 × 49.5 mm (cathode), and thicknesses of 0.136 mm and 0.155 mm, respectively. The N/P ratio was approximately 1.1. The SOC of $LiFePO_4$/graphite pouch cells was set using a NEWARE CT-5080-5V6A-ATL battery testing system (Shenzhen, China). To achieve the target SOCs of 50% and 75%, cells were charged under low current conditions to the corresponding voltages, followed by brief rest periods to ensure stabilization. After storage at 55 °C for one year under the specified SOCs, the cells were subjected to long-term cycling tests at room temperature to evaluate performance degradation. Each cycle consisted of a 1 C constant-current (CC) charge to 3.65 V, followed by a constant-voltage (CV) step at 3.65 V until the current declined to 0.05 C. After a 1-hour rest, cells were discharged at 1 C to 2.5 V, followed by another 1-hour rest before the next cycle. To further evaluate internal resistance evolution, electrochemical impedance spectroscopy (EIS) measurements were conducted using a Biologic VSP-3e workstation (France) at 25 °C, with a 5 mV amplitude over a frequency range of 0.01 Hz to 100 kHz.

Material Characterization

X-ray diffraction (XRD) patterns were collected using a Rigaku Ultima IV diffractometer equipped with Cu Kα radiation ($\lambda = 1.5405$ Å), operating at 40 kV and 30 mA. Data were acquired over a 2θ range of 10–90° with a scanning rate of $10° \text{ min}^{-1}$. Sample morphology was examined using a SUPRA55 scanning electron microscope (SEM), while surface chemical composition was analyzed via X-ray photoelectron spectroscopy (XPS) using a Thermo Scientific K-Alpha system. High-resolution transmission electron microscopy (HRTEM, JEM-2100, JEOL) and energy-dispersive

X-ray spectroscopy (TEM-EDXS) were employed to assess the microstructure of the electrode powders. Atomic force microscopy (AFM, Bruker Multimode 8) was used to probe the elastic modulus maps. Time-of-flight secondary ion mass spectrometry (TOF-SIMS) was conducted using an IONTOF M6 system (ION-TOF GmbH, Münster, Germany); a Bi^+ primary ion beam was used to acquire 3D maps over a 100 × 100 μm area, with a sputtering rate equivalent to 0.2 nm/s in SiO_2. Given the high sensitivity of SEI layers to air exposure, samples for XPS and TOF-SIMS were transferred from the glovebox to the analysis chamber via a dedicated vacuum-sealed transfer module. In situ thickness and gas evolution measurements were performed using the SWE2110 systems (Initial Energy Science & Technology Co., Ltd., Xiamen, China). Electrode electronic conductivity was evaluated using an electrode resistance tester (BER2500, IEST).

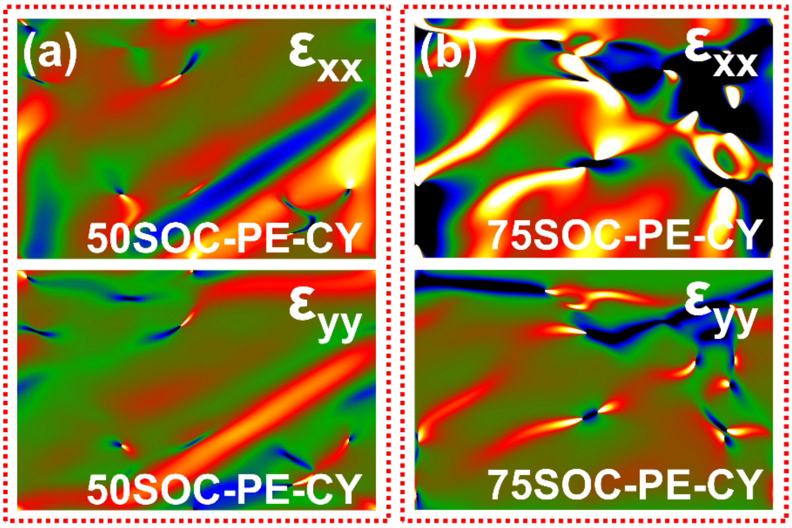

Fig S1. (a-b) Stress distribution images of the cell positive electrode after cycling.

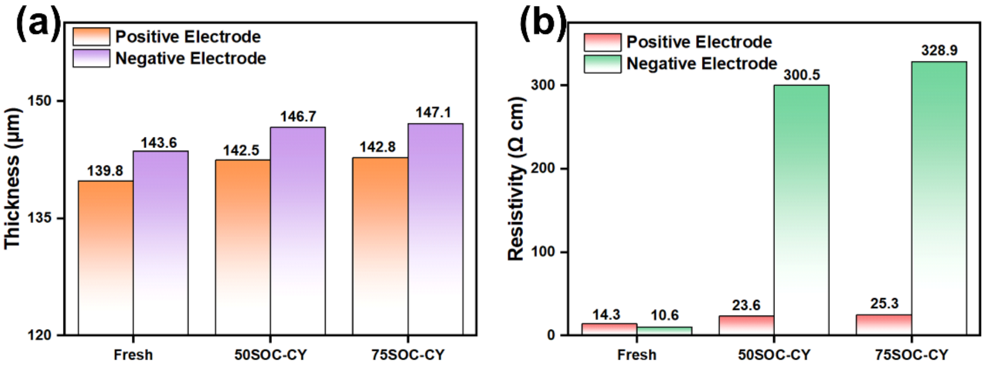

Fig S2. Changes in the (a) thickness and resistivity (b) of the positive electrode and negative electrode after cycling.

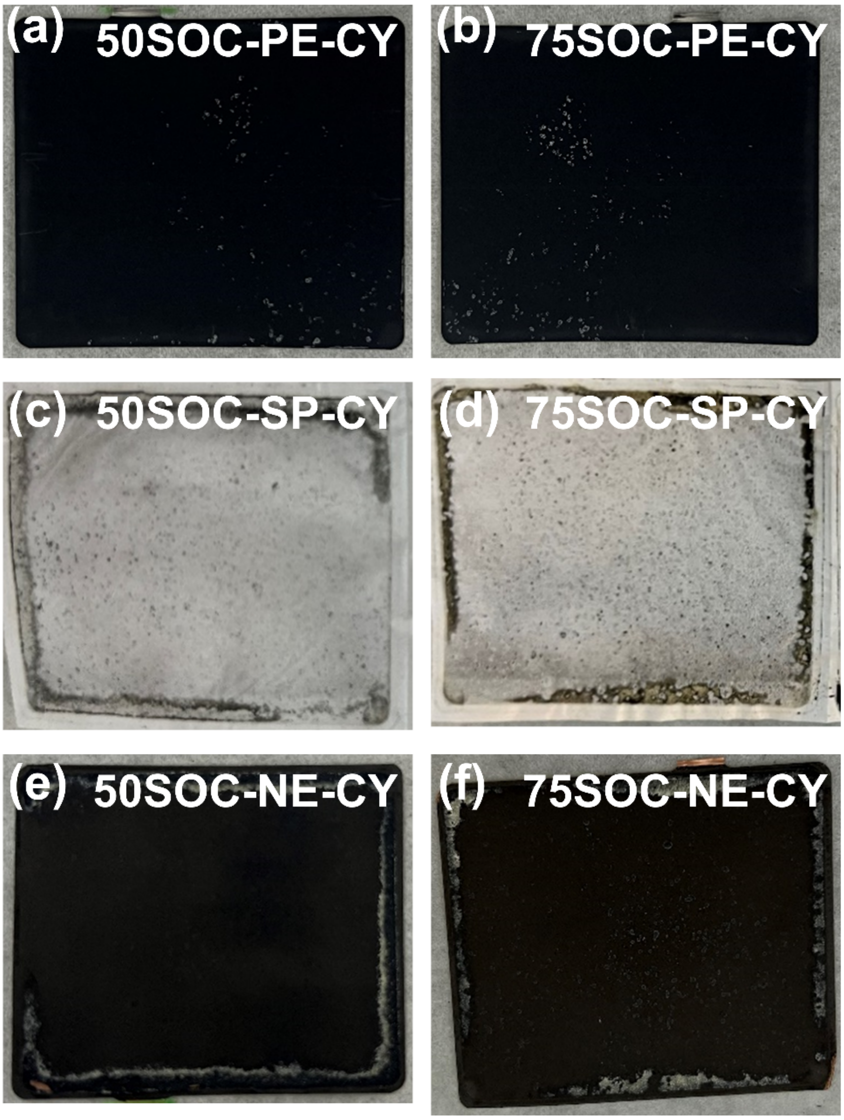

Fig S3. Images of (a) 50SOC-PE-CY, (b) 75SOC-PE-CY, (c) 50SOC-SP-CY, (d) 75SOC-SP-CY, (e) 50SOC-NE-CY, (f) 75SOC-NE-CY.

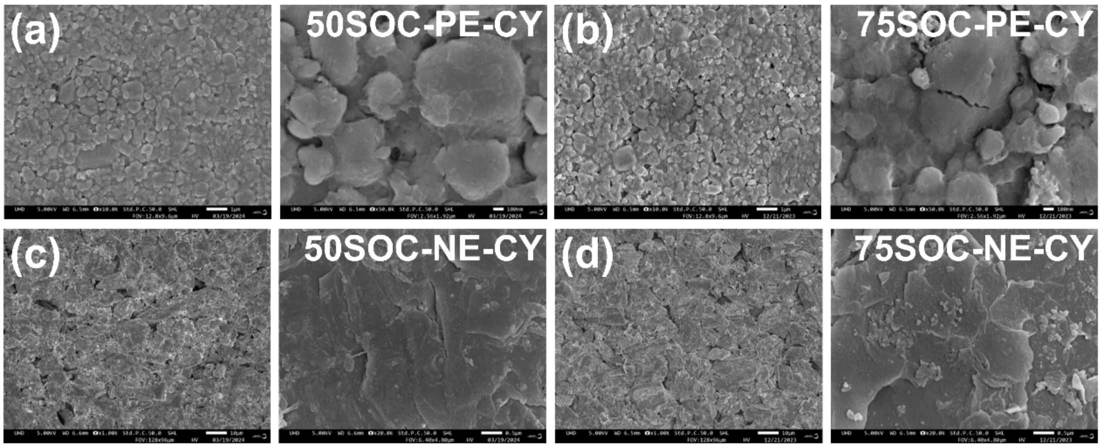

Fig S4. SEM images of (a) 50SOC-PE-CY, (b) 75SOC-PE-CY, (c) 50SOC-NE-CY, (d) 75SOC-NE-CY.

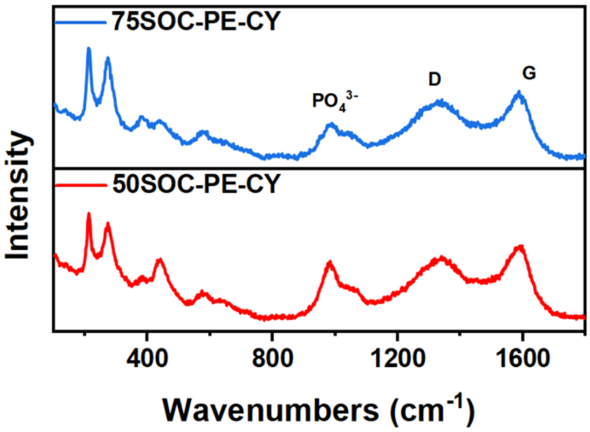

Fig S5. Raman spectra of positive electrode from 50SOC-PE-CY and 75SOC-PE-CY.

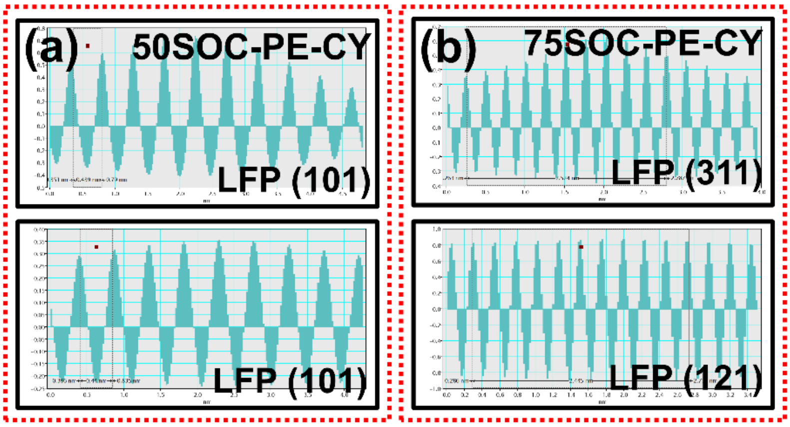

Figure S6. (a) The interplanar spacing of (101) plane of 50SOC-PE-CY. (b) The interplanar spacing of (311) plane and (121) plane of 75SOC-PE-CY.

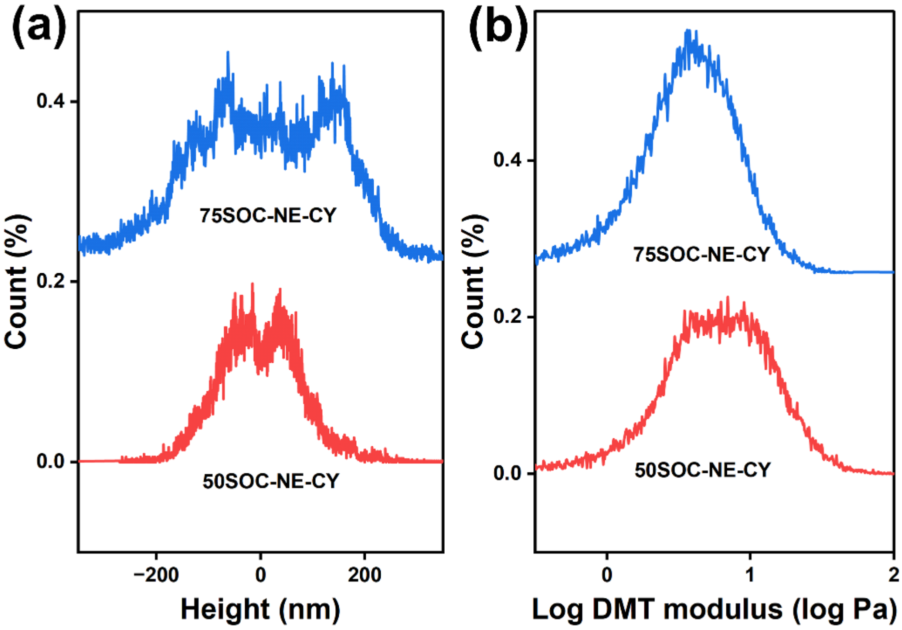

Figure S7. (a) Corresponding height and (b) Young’s modulus distribution comparison.

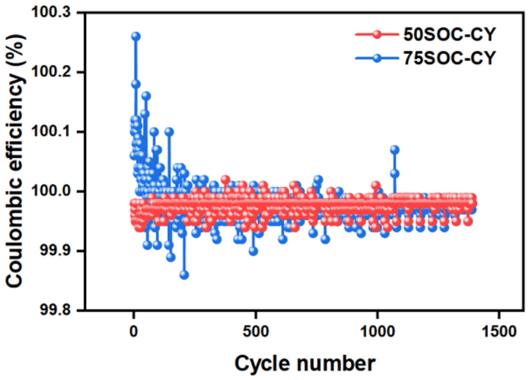

Figure S8. The Coulombic efficiency of batteries after being stored at different SOCs. a) 50SOC-CY, b) 75SOC-CY.

Figure S8 presents the CE of batteries cycled after storage at different SOC conditions. Both battery types demonstrate a CE above 99%, with some cycles even exceeding 100%. Notably, the CE of 75SOC-CY exhibits significant fluctuations, particularly in the initial cycles, whereas 50SOC-CY maintains a more stable CE throughout. Specifically, a correlation heatmap was constructed to visualize the interdependence of critical aging indicators, including capacity retention (CR), and direct current internal resistance (DCIR), as shown in figure S9. The results reveal strong statistical associations among these factors, confirming that lithium depletion, structural disintegration, and internal resistance accumulation co-evolve during rate-induced degradation.

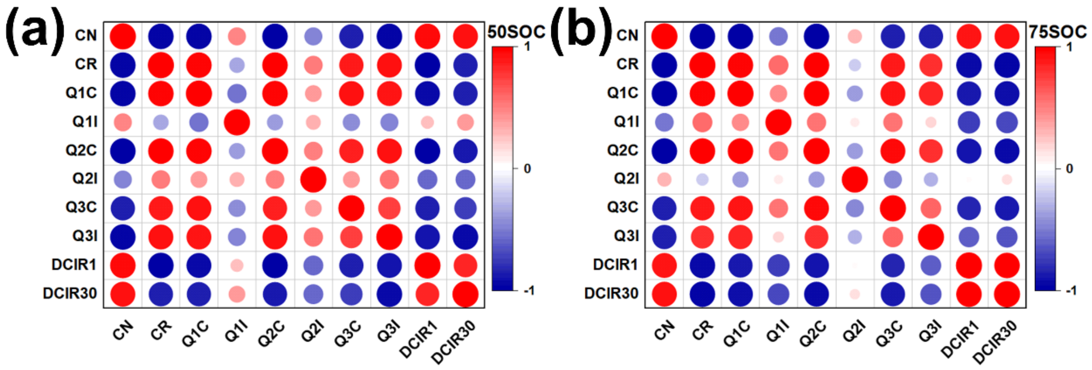

Figure S9. Correlation heatmap of different parameters during storage at (a) 50SOC, (b) 75SOC. CN represents cycling number, CR represents capacity retention. Q1C and Q1I indicate the horizontal and vertical changes of the QI peak in the DV curve, respectively. Q2C and Q2I correspond to the QII peak, while Q3C and Q3I correspond to the QIII peak. DCIR1 and DCIR30 represent the direct current internal resistance at 1 second and 30 seconds, respectively.

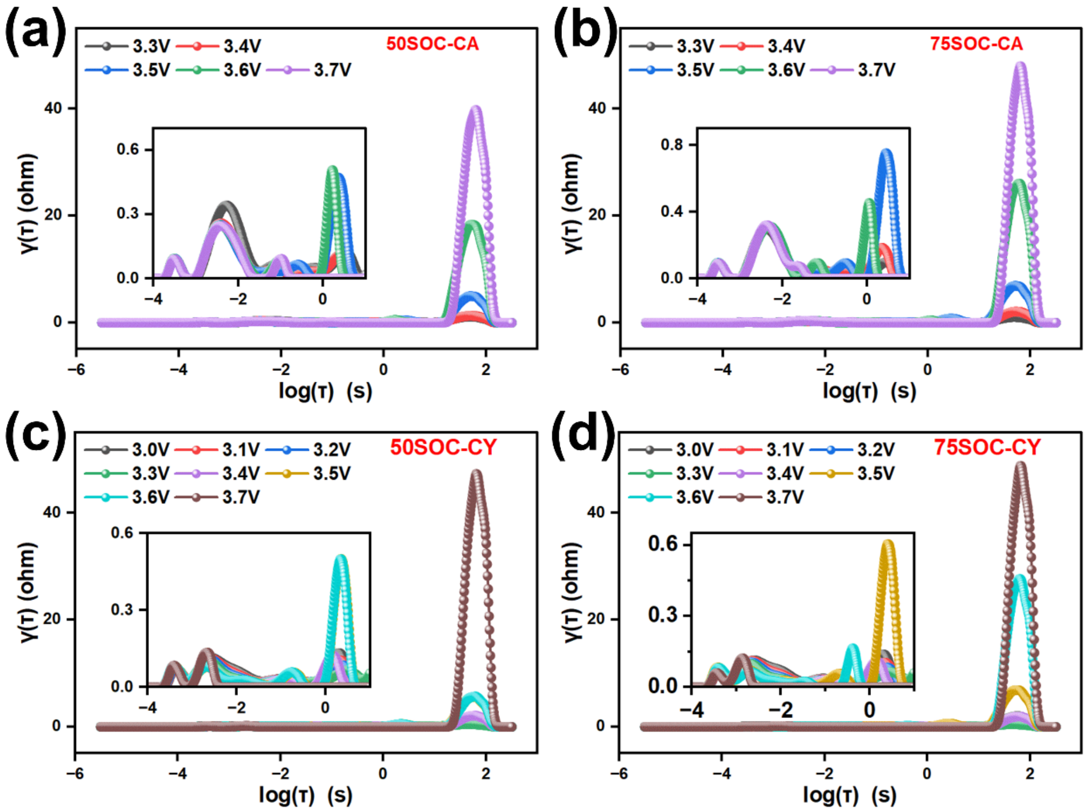

Figure S10. Static EIS test results with corresponding DRT plots of anode impedance at a) 50SOC-CA, b) 75SOC-CA, c) 50SOC-CY and d) 75SOC-CY.

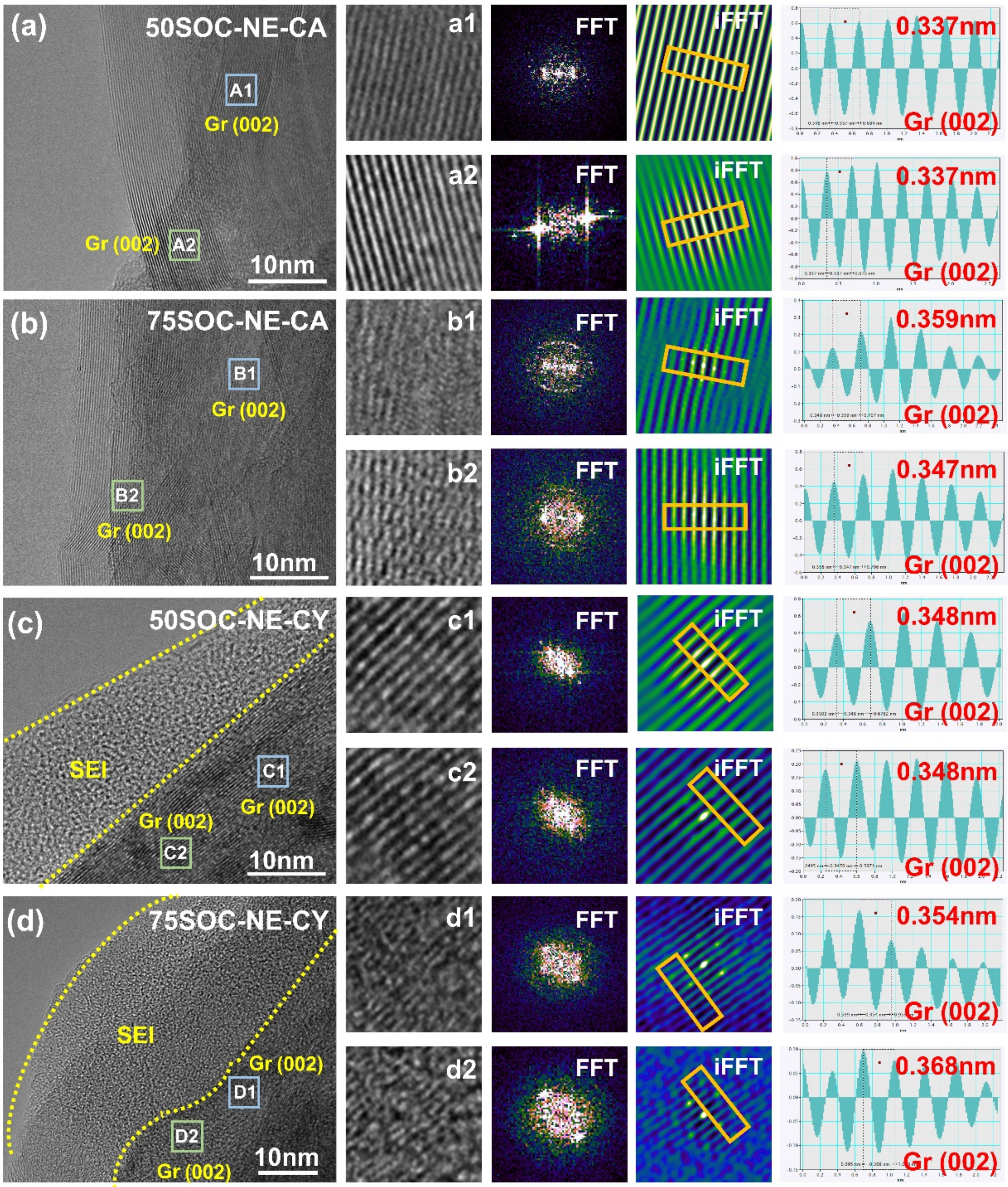

Figure S11. Structural evolution and characterization of powder microstructure during long-term high-temperature storage. HRTEM images and the corresponding FFT/ iFFT images of (a) 50SOC-NE-CA, (b) 75SOC-NE-CA, (c) 50SOC-NE-CY, (d) 75SOC-NE-CY.

Table S1. The Rietveld refinement results of different cathodes.

Sample	**Phase**	**Space**	**a (Å)**	**b (Å)**	**c (Å)**	**V (Å3)**	**Wt.**	χ^2
50SOC-PE-CA	LFP	Pnma	10.31839	6.00315	4.69169	290.617	0.753	2.05
	FP	Pnma	9.81567	5.79016	4.78453	271.925	0.247	
75SOC-PE-CA	LFP	Pnma	10.32035	6.00336	4.6915	290.670	0.388	1.98
	FP	Pnma	9.81777	5.79081	4.78419	271.995	0.612	
50SOC-SPE-CA	LFP	Pnma	10.31825	6.00229	4.692	290.590	0.72	1.45
	FP	Pnma	9.81445	5.78972	4.78399	271.840	0.28	
75SOC-SPE-CA	LFP	Pnma	10.47084	6.09547	4.94033	315.315	0.14	3.11
	FP	Pnma	9.81897	5.79289	4.78583	272.219	0.86	

Table S2. XPS analysis of the C 1s spectra.

	50SOC-NE-CA/%	75SOC-NE-CA/%	50SOC-SNE-CA/%	75SOC-SNE-CA/%
CO_3^{2-}	25.58	12.2	24.46	10.36
C=O	7.7	18.84	11.61	10.69
C-O	23.51	15.67	26.71	44.63
C-C/C-H	43.21	25.47	37.22	34.32
Li_xC	——	27.82	——	——

Table S3. XPS analysis of the F 1s spectra.

	50SOC-NE-CA/%	75SOC-NE-CA/%	50SOC-SNE-CA/%	75SOC-SNE-CA/%
P-F	41.73	83.66	73.84	31.53
Li-F	58.27	16.34	26.16	68.47

Table S4. XPS analysis of the O 1s spectra.

	50SOC-NE-CA/%	75SOC-NE-CA/%	50SOC-SNE-CA/%	75SOC-SNE-CA/%
C-O	17.08	57.53	36.68	27.7
CO_3^{2-}	82.92	42.47	63.32	72.3

Table S5. XPS analysis of the P 2p spectra.

	50SOC-NE-CA/%	75SOC-NE-CA/%	50SOC-SNE-CA/%	75SOC-SNE-CA/%
P-F	22.38	42.42	64.69	35.18
P-O/P=O$^-$	77.62	57.58	35.31	64.82